To appear in *Remote Sensing Letters*
Vol. 00, No. 00, Month 20XX, 1–10

Enhancing the Temporal Resolution of Image Sequences Capturing Evolving Weather Phenomena

I. Yanovsky[a,b*] and B. Lambrigtsen[a]

[a] *Jet Propulsion Laboratory, California Institute of Technology, Pasadena, CA 91109, USA;* [b] *University of California, Los Angeles, Joint Institute for Regional Earth System Science and Engineering, Los Angeles, CA 90095, USA*

(*November 16, 2015*)

In this article, we develop an approach for temporal resolution enhancement of blurry and distorted image sequences capturing evolving weather phenomena. We first enhance the spatial resolution of a sequence of images using an efficient deconvolution method which we showed to reduce image ringing, blurring, and distortion, while sharpening the image and preserving information content. Such methodology is based on current research in sparse optimization and compressed sensing, which lead to unprecedented efficiencies for solving image reconstruction problems. We then consider the evolving sequence to be embedded in a deformable medium, and enhance temporal resolution of a sequence using nonlinear viscous fluid registration model. The physical continuum equation is solved using an efficient multigrid full approximation scheme.

1. Introduction

Temporal resolution enhancement is important in the studies of physically evolving phenomena, such as hurricanes and tropical storms. Such weather phenomena will soon be continuously captured using geostationary microwave sensors. These sensors are designed to penetrate through thick clouds to see the structure of a storm. The images collected are valuable for evaluating the storm's internal processes and its strength.

Temporal resolution specifies the revisiting frequency of a satellite sensor for a specific location, or equivalently, refers to how often an area can be imaged by a sensor. In other words, temporal resolution defines the time interval between consecutive captured frames. It also relates to the duration of time for acquisition of a single frame of a dynamic process.

Spatial resolution, on the other hand, is conceptually different from temporal resolution. Spatial resolution is a measure of how fine an image is and often specifies the pixel size of satellite images covering the earth surface. For blurry and distorted imagery, spatial resolution is coarser than the pixel size of an image. For remotely sensed imagery, spatial resolution refers to the smallest feature that can be resolved in the image.

*Corresponding author. Email: igor.yanovsky@jpl.nasa.gov. This is an Accepted Manuscript of an article published by Taylor & Francis in Remote Sensing Letters on December 23, 2015, available at http://www.tandfonline.com/doi/full/10.1080/2150704X.2015.1128130.

There is often a tradeoff between temporal resolution of a measurement and its spatial resolution. Acquiring a high spatial resolution image requires more time, which inadvertently affects temporal resolution of a sequence. On the other hand, spatial resolution is affected if images are acquired quickly. Both spatial resolution and temporal resolution enhancements are challenging inverse problems. Conceptual diagram depicting spatial and temporal resolution enhancement processes is shown on Figure 1.

In our studies, we consider the Geostationary Synthetic Thinned Aperture Radiometer (GeoSTAR) (Tanner et al. 2007), which is a microwave spectrometer aperture synthesis system that will be used to capture hurricane imagery and other evolving weather phenomena. A characteristic of an aperture synthesis system is that the point spread function (PSF) is a 2-dimensional sinc-like function, showing positive and negative excursions (cf. Fig. 2(a,b)), that produces ringing at sharp edges and other transitions in the observed field. The conventional approach to suppressing such sidelobes is to apply linear apodization, which has the undesirable side effect of degrading spatial resolution (Tanner and Swift 1993; Yanovsky et al. 2015).

In Section 2, we use sparsity-based approaches to first enhance *spatial resolution* of image sequence. In order to reduce image ringing while sharpening the image and preserving information content, we formally solved the deconvolution inverse problem for single-channel images in (Yanovsky et al. 2015). Since the convolution problem is highly ill-posed, regularization was applied to achieve stability while preserving a priori properties of the solution. We formulated the restoration problem within the variational framework, using the total variation regularization (Rudin, Osher, and Fatemi 1992). Total variation (TV) of an image measures the sum of the absolute values of its gradient and increases in the presence of the ringing artifact caused by sidelobes. By minimizing the TV, we showed that the process reduces not only the ringing within the image, but also significantly reduces the brightness temperature errors in the overall image. These processes were rendered efficiently by employing methodologies based on current research in sparse optimization and compressed sensing.

In Section 3, we describe the methodology to enhance *temporal resolution* of image sequences capturing evolving weather phenomena. Given a pair of spatially resolved frames, we solve an image registration problem in order to find an unknown intermediate frame. An important observation, which stimulated the development of intensity-based nonlinear image registration algorithms, was the connection of the image data with a physically deforming system. Physical continuum models consider the deforming image to be embedded in a deformable medium, which can be either an elastic material or a viscous fluid. We use the viscous fluid registration in order to temporally resolve multiframe sequence of images.

In our experiments, we use simulated microwave images of Atlantic hurricane Rita, which was active in the Gulf of Mexico between 18 and 26 September 2005. The real image, captured by the Moderate-resolution Imaging Spectroradiometer (MODIS) instrument on board the Terra Satellite at 4:55 PM GMT on 22 September 2005, is shown in Figure 2(c).

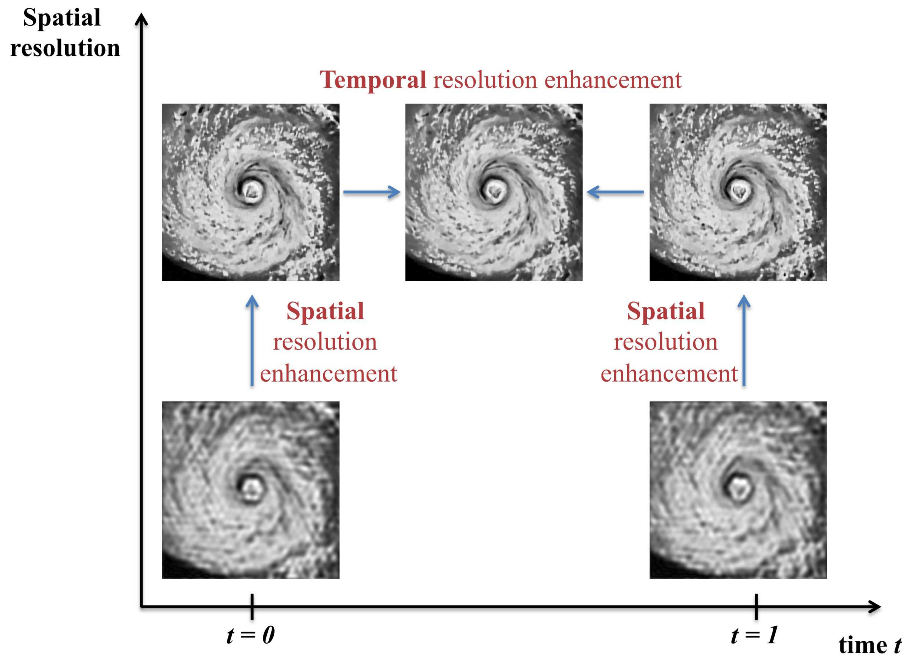

Figure 1. Conceptual diagram of spatial and temporal resolution enhancements.

2. Efficient Deconvolution

A deconvolution process reverses the effects of a blurring sensor PSF on observed data in the presence of noise. Let Ω be an open and bounded domain in $\mathbb{R}^2$. Let $I_0 : \Omega \to \mathbb{R}$ be an original unknown image, K be a convolution operator that represents the point spread function, and κ be additive noise. A blurred, distorted, and noisy observation J satisfies the model

$$J = K * I_0 + \kappa, \tag{1}$$

where $*$ denotes convolution. For an aperture synthesis system, K is a sinc-like point spread function which introduces sidelobes in the observation. Rather than apply the conventional linear apodization approach, which has the undesirable side effect of degrading spatial resolution (Tanner and Swift 1993; Yanovsky et al. 2015), we suppress interferometric sidelobes by constructing a variational formulation for image reconstruction and solving an inverse problem. Regularization is applied within a variational framework in order to achieve stability while preserving a priori properties of the solution.

In (Yanovsky et al. 2015), we formulated the restoration problem within the variational framework, using the total variation regularization. The L_1-regularized type norm $||I||_{\mathrm{TV}} = \int |\nabla I|$ measures TV of a signal (Rudin, Osher, and Fatemi 1992). Given an observation J, we solve the inverse problem related to (1). That is, we find a suitable approximation of the original unknown image I by means of the solution of the following TV-L_2 minimization problem

$$\min_I \quad ||I||_{\mathrm{TV}} + \frac{\mu}{2}||K * I - J||_2^2, \tag{2}$$

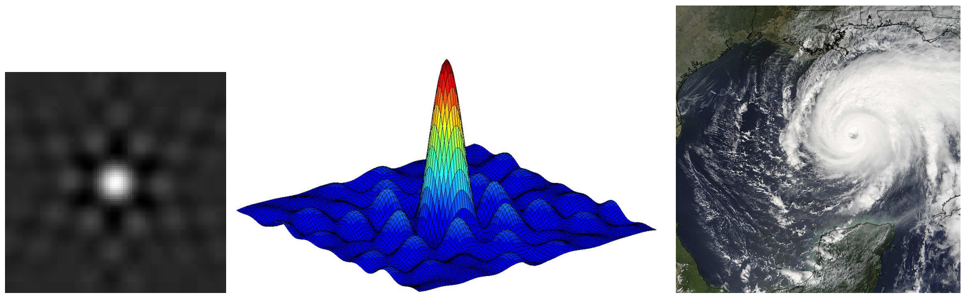

(*a*) (*b*) (*c*)

Figure 2. (*a*) The GeoSTAR PSF shown as image. A characteristic of an aperture synthesis system is that the PSF is a 2-dimensional sinc-like function, showing positive and negative excursions, that produces ringing at sharp edges and other transitions in the observed field. (*b*) The GeoSTAR PSF shown as surface. (*c*) Terra MODIS image of hurricane Rita in the Gulf of Mexico captured at 4:55 PM GMT on 22 September 2005. Image Credit: NASA/GSFC, MODIS Rapid Response.

where $\mu > 0$. The value of μ can be calculated automatically via Bregman iteration (Yin et al. 2008; Osher et al. 2005). We solve (2) using Split Bregman (Goldstein and Osher 2009) deconvolution model where the equation for I is re-written in the fast Fourier Transform formulation framework (Yanovsky et al. 2015).

3. Registration Problem

Let $I_1 : \Omega \to \mathbb{R}$ and $I_2 : \Omega \to \mathbb{R}$ be the two images to be registered. Both I_1 and I_2 were independently reconstructed using the process of Section 2 from blurry observations J_1 and J_2, respectively. The goal of image registration is to find the transformation $\boldsymbol{g} : \Omega \to \Omega$ that maps the source image I_2 into correspondence with the target image I_1. The displacement field $\boldsymbol{u}(\boldsymbol{x})$ from the position $\boldsymbol{x}$ in the deformed image $I_2 \circ \boldsymbol{g}(\boldsymbol{x})$ back to $I_2(\boldsymbol{x})$ is defined in terms of the deformation $\boldsymbol{g}(\boldsymbol{x})$ by the expression $\boldsymbol{g}(\boldsymbol{x}) = \boldsymbol{x} - \boldsymbol{u}(\boldsymbol{x})$ at every point $\boldsymbol{x} \in \Omega$. The term displacement is used because it can be viewed as how a point in the deformed template is moved away from its original location. Thus, the problems of finding deformation $\boldsymbol{g}$ and displacement $\boldsymbol{u}$ are equivalent.

3.1. *Registration Metric*

Images acquired using the same or similar sensors are expected to present the same intensity range and distribution. For registration of such images, the most common way to define the distance between the deformed source and the target images is to use the L^2 norm, or the sum of squared differences (SSD). Alternatively, if evolutionary mechanisms such as growth and decay of image intensity is needed to be modeled, mutual information between the images could be considered.

The L^2 distance between the deformed image $I_2(\boldsymbol{x} - \boldsymbol{u})$ and target image $I_1(\boldsymbol{x})$ is defined as

$$F_{L^2}(I_1, I_2, \boldsymbol{u}) = \frac{1}{2}\big|\big|I_2(\boldsymbol{x} - \boldsymbol{u}) - I_1(\boldsymbol{x})\big|\big|_{L^2(\Omega)} = \frac{1}{2}\int_\Omega \big(I_2(\boldsymbol{x} - \boldsymbol{u}) - I_1(\boldsymbol{x})\big)^2 \,\mathrm{d}\boldsymbol{x}. \quad (3)$$

Computing the first variation of the L^2 similarity functional F_{L^2} with respect to variations of the displacement field $\boldsymbol{u}$ gives

$$\boldsymbol{f}(\boldsymbol{x}, \boldsymbol{u}(\boldsymbol{x})) = -\partial_{\boldsymbol{u}} F_{L^2}(I_1, I_2, \boldsymbol{u}) \;=\; [I_2(\boldsymbol{x} - \boldsymbol{u}(\boldsymbol{x})) - I_1(\boldsymbol{x})]\, \nabla I_2|_{\boldsymbol{x}-\boldsymbol{u}}, \tag{4}$$

where $\boldsymbol{f}$ is the force field, or the body force, which drives the source into registration with the target. The first term in the definition of $\boldsymbol{f}$, namely $I_2(\boldsymbol{x} - \boldsymbol{u}) - I_1(\boldsymbol{x})$, is the difference in intensity between the deformed image and the target image. This term causes the field force to tend to zero in areas where the deformed source image is locally aligned with the target image. The second term $\nabla I_2|_{\boldsymbol{x}-\boldsymbol{u}}$ is the gradient of the deformed source image and has largest values at the edges of the source image. This term determines the directions of the local deformation forces applied to the source.

The minimization of (3), however, is known to be ill-posed. In particular, the displacement field $\boldsymbol{u}$ is not unique, and the regularization on $\boldsymbol{u}$ is required to make the problem be well-posed. We now review approaches to regularizing the displacement field.

3.2. *Physical Continuum Models*

An important observation, which stimulated the development of intensity-based nonlinear image registration algorithms, was the connection of the image data with a physically deforming system (Thompson and Toga 2002). Physical continuum models consider the evolving image to be embedded in a deformable medium, which can be either an elastic material or a viscous fluid. The medium is subjected to certain distributed internal forces, which reconfigure the medium and eventually drive the source into registration with the target. We briefly describe two of the most well known such models.

3.2.1. Elastic Registration

Bajcsy and Kovacic (1989); Broit (1981); Dann et al. (1989) noticed the similarity between image deformation and deformation of elastic plates. For linear elastic solids, the force field $\boldsymbol{f}$ is proportional to the displacement field $\boldsymbol{u}$. The spatial transformation satisfies the Navier-Cauchy linear elastic partial differential equation

$$\mu \triangle \boldsymbol{u} + (\mu + \nu)\nabla(\nabla \cdot \boldsymbol{u}) + \boldsymbol{f}(\boldsymbol{x}) = 0, \tag{5}$$

where μ and ν are Lamé constants, describing the properties of the material.

3.2.2. Viscous Fluid Registration

A major shortcoming of the linear elastic approach using Navier-Cauchy equations (5) is that it is based on the assumption of an infinitesimally small deformation. Large deformations can not be accommodated with these linear partial differential equations. The limitations of the linear elasticity model can be overcome by a viscous fluid which allows the restoring forces to relax over time.

In the viscous fluid model, first proposed by Christensen, Rabbitt, and Miller (1996), an Eulerian reference frame is used in describing large deformations. The Eulerian frame of reference specifies the time evolution of particle positions and velocities as observed at fixed points. Consequently, a particle located at $\boldsymbol{x}$ at time

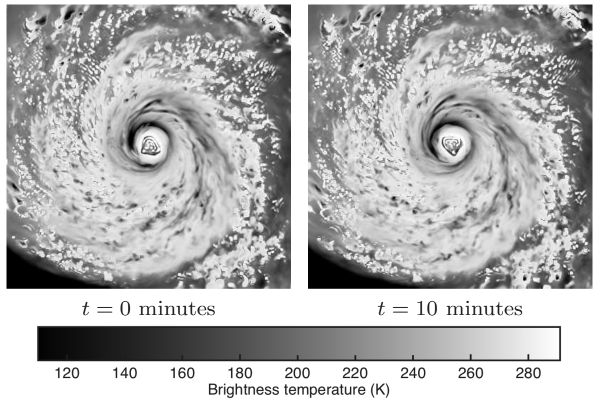

Figure 3. Original 150GHz microwave 400×400 pixel images of the simulated hurricane Rita at time 12:00 AM GMT and 12:10 AM GMT.

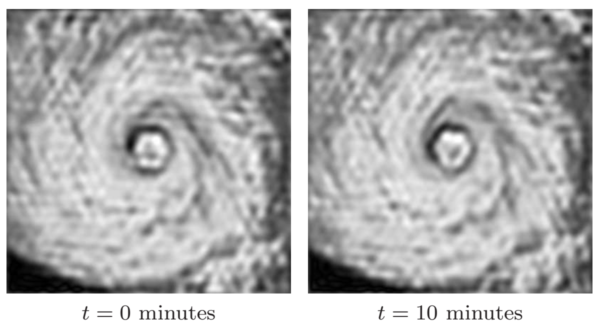

Figure 4. Original images from Figure 3 are convolved with the GeoSTAR kernel and corrupted with noise κ from equation (1). The standard deviation of the noise, σ, was equal to 2K.

t originated at position

$$\boldsymbol{g}(\boldsymbol{x}, t) = \boldsymbol{x} - \boldsymbol{u}(\boldsymbol{x}, t) \tag{6}$$

at time t_0 ($t > t_0$), where $\boldsymbol{u}$ is the displacement. We let $\boldsymbol{v}$ denote the velocity field. The material derivative, defined by $\mathrm{D}/\mathrm{D}t = \partial/\partial t + \boldsymbol{v} \cdot \nabla$, describes the time rate of change experienced by an element of material instantaneously at point $\boldsymbol{x}$ at time t. Hence, the Eulerian velocity field $\boldsymbol{v}$ is nonlinearly related to $\boldsymbol{u}$ and is determined by

$$\boldsymbol{v} = \frac{\mathrm{D}\boldsymbol{u}}{\mathrm{D}t} = \frac{\partial \boldsymbol{u}}{\partial t} + \boldsymbol{v} \cdot \nabla \boldsymbol{u}. \tag{7}$$

The term $\boldsymbol{v} \cdot \nabla \boldsymbol{u}$ accounts for the kinematic nonlinearities of the displacement field $\boldsymbol{u}$. Note that the material derivative with respect to time t and partial derivative with respect to time t are approximately equal for small deformations.

Given the velocity field $\boldsymbol{v}$, equation (7) can be solved to obtain the displacement field $\boldsymbol{u}$. Christensen, Rabbitt, and Miller (1996) considered the deforming template image to be embedded in a viscous fluid whose motion is governed by Navier-Stokes equation for conservation of momentum. Some simplification of the momentum conservation equation resulted in the following equation for the unknown variable $\boldsymbol{v}$:

$$\mu \triangle \boldsymbol{v} + (\mu + \nu) \nabla (\nabla \cdot \boldsymbol{v}) + \boldsymbol{f}(\boldsymbol{x}, \boldsymbol{u}) = 0. \tag{8}$$

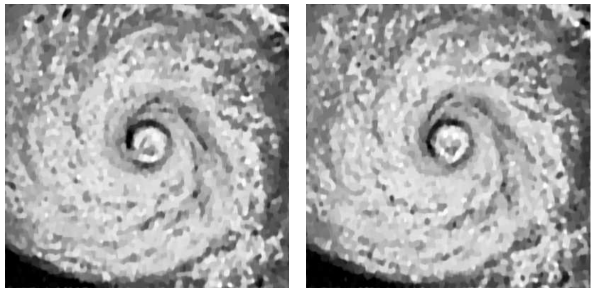

$t = 0$ minutes (image I_2) $t = 10$ minutes (image I_1)

Figure 5. Spatial resolution enhancement of images from Figure 4.

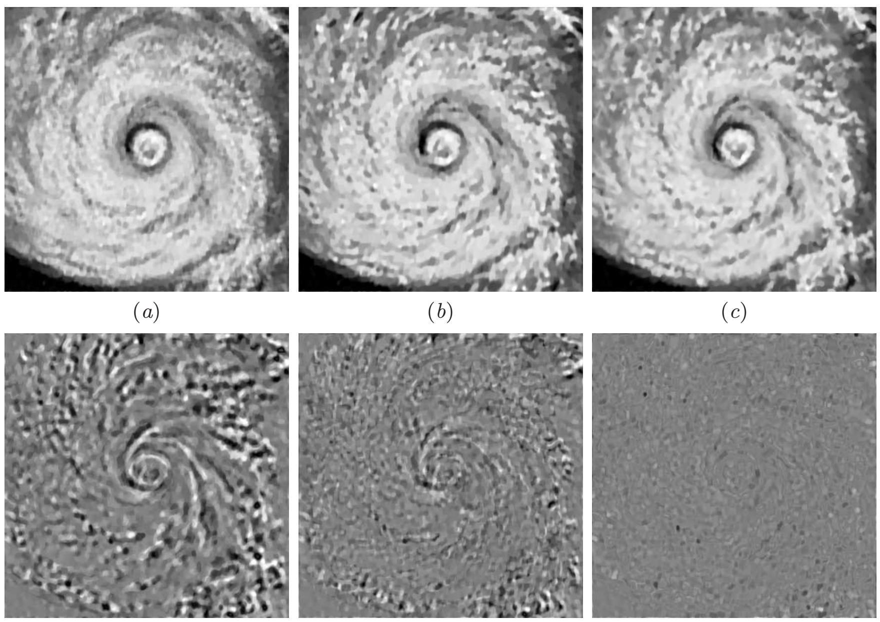

(*a*) (*b*) (*c*) (*d*) (*e*) (*f*)

Figure 6. (*a*) Linear interpolation between I_1 and I_2 for time = 5 minutes. (*b*) Image I_2 defined at time = 0 (see Fig. 5) is deformed to time = 5 minutes. (*c*) Image I_2 is deformed to match image I_1 at time = 10 minutes. (*d*) Difference between I_1 (time = 10 minutes) and I_2 (time = 0). (*e*) Difference between I_1 and $I_2 \circ \boldsymbol{g}(t = 5 \text{ minutes})$ (*f*) Difference between I_1 and $I_2 \circ \boldsymbol{g}(t = 10 \text{ minutes})$ indicating close match between image I_1 and image I_2 after deformation.

Equation (8) describes the balance of forces acting in a given region of the fluid. The $\triangle \boldsymbol{v}$ term is the viscosity, which constraints the velocity field to vary smoothly. The term $\nabla(\nabla \cdot \boldsymbol{v})$ allows structures in the source image to change in mass. The Navier-Stokes equation of fluid flow (8) is identical to the Navier-Cauchy equation of linear elasticity (5) except that the Navier-Stokes partial differential equation operates on velocity $\boldsymbol{v}$ rather than displacement $\boldsymbol{u}$.

Equation (8) is computationally expensive to solve in practice using conventional techniques. Christensen, Rabbitt, and Miller (1996) used successive over relaxation (SOR) to solve (8), which is still inefficient for larger images. D'Agostino et al. (2003) proposed to simplify the problem, obtaining the instantaneous velocity from the convolution of $\boldsymbol{f}$ with Gaussian kernel G. We solve (8) very efficiently using the multigrid full approximation scheme (Brandt 1977).

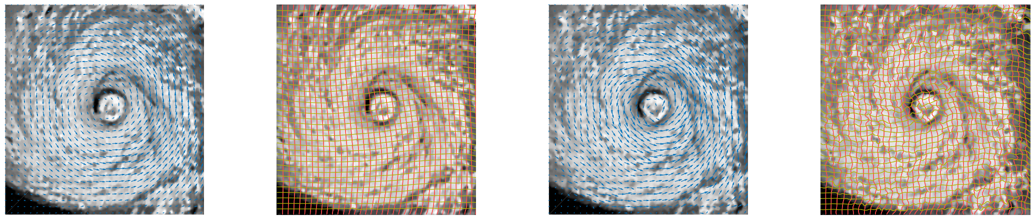

(a) $t = 5$ minutes (b) $t = 5$ minutes (c) $t = 10$ minutes (d) $t = 10$ minutes

Figure 7. Displacement fields and deformation grids generated as image I_2 is deformed to match image I_1. Deformation at intermediate and final stages are shown.

4. Results

Figure 1 shows a conceptual diagram of spatial and temporal resolution enhancements. Spatial resolution enhancement is performed first for each image in a temporal sequence. Temporal resolution is performed next using the nonlinear viscous fluid registration model.

4.1. *Spatial Resolution Enhancement*

We performed spatial resolution enhancement of Section 2 on simulated microwave 150 GHz channel images of the 2005 Atlantic hurricane Rita, shown in Figure 3. For comparison, GeoSTAR operates at some of the same frequencies of the Advanced Microwave Sounding Unit - B (AMSU-B) temperature and humidity sounders near 180 GHz. The images are 400×400 pixels and were derived from cloud resolving numerical weather prediction model (WRF) (Michalakes et al. 1998) simulations. Each pair of images is captured 10 minutes apart. The resolution of a pixel is 1.3 km. With this grid spacing, we can resolve features that are approximately 5 km wide. We used the 101×101 GeoSTAR point spread function K, which has a full width at half maximum of 27.6 km and is shown in Figure 2 (a,b), to blur the images.

Figure 4 shows a pair of 150 GHz images of Figure 3 degraded with the GeoSTAR blur and corrupted with additive image noise κ from equation (1) of standard deviation $\sigma = 2K$. The result in Figure 5 is obtained using the efficient Split Bregman deconvolution model (Yanovsky et al. 2015).

4.2. *Temporal Resolution Enhancement*

In this section, we show temporal resolution enhancement of a sequence containing consecutive images I_2 and I_1, shown in Figure 5, at times 0 and 10 minutes, respectively. The goal of temporal resolution is to recover a representation of the evolving phenomenon at intermediate time (e.g. 5 minutes).

We first perform linear interpolation between the two images from Figure 5 in order to reconstruct intermediate image at time = 5 minutes. As shown on Figure 6(a) linear interpolation smooths out features of the hurricane visible on Figure 5. On the other hand, nonlinear viscous fluid registration deforms image I_2, originally defined at time 0, continuously moving through intermediate stages of deformation, while preserving the structure of the hurricane, until it matches image I_1 at time 10 minutes. Figure 6(b) shows image I_2 deformed to time = 5 minutes, which is the time we seek to have a valid frame. In Figure 6(c), image I_2 is deformed to match image I_1 at time = 10 minutes. Figure 6(d) shows difference between I_1 and I_2. Figure 6(e) shows difference between I_1 and $I_2 \circ \boldsymbol{g}(t = 5 \text{ min})$ and Figure 6(f) shows difference between I_1 and $I_2 \circ \boldsymbol{g}(t = 10 \text{ min})$ indicating that the algorithm is capable of generating close matches for physical processes. We note that the performance of the temporal interpolator has only been tested on one pair of images 10 minutes apart, and without quantitative performance assessment. This technique may not work well for intervals longer than 10 minutes.

Figure 7 shows displacement fields and deformation grids generated as image I_2 is deformed to match image I_1. Deformation at intermediate and final stages are shown.

5. Conclusions

We developed an approach for temporal resolution enhancement of blurry and distorted image sequences capturing evolving weather phenomena. In our studies, we considered the GeoSTAR instrument, which is a microwave spectrometer aperture synthesis system that will be used to capture hurricane imagery and other evolving weather phenomena. We used sparsity-based approaches to first enhance spatial resolution of image sequence. In order to reduce image ringing while sharpening the image and preserving information content, we formally solved the deconvolution inverse problem for single-channel images. We then described the methodology to enhance temporal resolution of image sequences capturing evolving weather phenomena. Given a pair of spatially resolved frames, we solve an image registration problem in order to find an unknown intermediate frame.

The GeoSTAR instrument is only one example for which our method is applicable. The method considered in this article can be applied to other types of remote sensing image sequences. The method is relevant in cases where there is oversampling and when the PSF is known.

Funding

The research was carried out at the Jet Propulsion Laboratory, California Institute of Technology, under a contract with the National Aeronautics and Space Administration. IY also acknowledges support from the National Science Foundation Grant DMS 1217239.

References

Bajcsy, R., and S. Kovacic. 1989. “Multiresolution Elastic Matching.” *Computer Vision Graphics and Image Processing* 46: 1–21.

Brandt, Achi. 1977. “Multi-Level Adaptive Solutions to Boundary-Value Problems.” *Mathematics of Computation* 31 (138): 333–390.

Broit, C. 1981. “Optimal Registration of Deformed Images.” Ph.D. thesis. University of Pennsylvania.

Christensen, G., R. Rabbitt, and M. Miller. 1996. “Deformable templates using large deformation kinematics.” *IEEE Transactions on Image Processing* 5 (10): 1435–1447.

D'Agostino, E., F. Maes, D. Vandermeulen, and P. Suetens. 2003. "A viscous fluid model for multimodal non-rigid image registration using mutual information." *Medical Image Analysis* 7: 565–575.

Dann, R., J. Hoford, S. Kovacic, M. Reivich, and R. Bajcsy. 1989. "Evaluation of Elastic Matching System for Anatomic (CT,MR) and Functional (PET) Cerebral Images." *Journal of Computer Assisted Tomography* 13: 603–611.

Goldstein, T., and S. Osher. 2009. "The Split Bregman Method for L1-Regularized Problems." *SIAM Journal on Imaging Sciences* 2 (2): 323–343.

Michalakes, J., J. Dudhia, D. Gill, J. Klemp, and W. Skamarock. 1998. *Design of a next-generation regional weather research and forecast model: Towards Teracomputing*. River Edge, New Jersey: World Scientific.

Osher, S., M. Burger, D. Goldfarb, J. Xu, and W. Yin. 2005. "An Iterative Regularization Method for Total Variation-Based Image Restoration." *Multiscale Modeling & Simulation* 4 (2): 460–489.

Rudin, L., S. Osher, and E. Fatemi. 1992. "Nonlinear Total Variation Based Noise Removal Algorithms." *Physica D* 60: 259–268.

Tanner, A.B., and C.T. Swift. 1993. "Calibration of a synthetic aperture radiometer." *IEEE Transactions on Geoscience and Remote Sensing* 31 (1): 257–267.

Tanner, A.B., W.J. Wilson, B.H. Lambrigsten, S.J. Dinardo, S.T. Brown, P.P. Kangaslahti, T.C. Gaier, et al. 2007. "Initial Results of the Geostationary Synthetic Thinned Array Radiometer (GeoSTAR) Demonstrator Instrument." *IEEE Transactions on Geoscience and Remote Sensing* 45 (7): 1947–1957.

Thompson, P., and A. Toga. 2002. "A framework for computational anatomy." *Computing and Visualization in Science* 5: 13–34.

Yanovsky, Igor, Bjorn Lambrigtsen, Alan Tanner, and Luminita Vese. 2015. "Efficient Deconvolution and Super-Resolution Methods in Microwave Imagery." *IEEE Journal of Selected Topics in Applied Earth Observations and Remote Sensing* .

Yin, W., S. Osher, D. Goldfarb, and J. Darbon. 2008. "Bregman Iterative Algorithms for L1-Minimization with Applications to Compressed Sensing." *SIAM Journal on Imaging Sciences* 1 (1): 143–168.